MULTISCIA
JOURNALS PUBLISHERS

FRONTIERS IN PHARMACEUTICAL ANALYSIS

ISSN: (3065- 1352)

https://multisciajournals.com/journals/index.php/fpa
editor.fpa1@gmail.com

Frontiers in Zoological Research
Volume 1 Issue 4 2025

Protein unique to the testis HSF5 is necessary for transcriptional reprogramming and appropriate chromatin architecture, which propel the development of pachynema.

R Kummari, C Bhagvati
Department of **Zoological Research**

Article Info

Received: 30-9-2025 Revised:08-11-2025 Accepted:19-11-2025 Published:29-11-2025

ABSTRACT

During mammalian meiotic prophase I, chromatin remodeling and transcriptional reprogramming are crucial processes, but the exact mechanisms governing these processes are still unclear. Our earlier research showed that male infertility and meiotic arrest are caused by the loss of heat shock factor 5 (HSF5), a member of the heat shock factor family. Nevertheless, the molecular mechanisms by which HSF5 controls meiotic development remain unclear. The function of HSF5 in regulating chromatin dynamics and transcriptional reprogramming during pachynema progression was examined in this work using a thorough multi-omics approach. Significant changes in chromatin accessibility and disruption of the transcriptional regulatory network (TRN) were found in Hsf5−/− spermatocytes, according to analysis of ATAC-seq and single-cell RNA sequencing data. Furthermore, poor XY body formation and abnormal histone modifications were caused by HSF5 loss. Significantly, Hsf5−/− spermatocytes also showed aberrant spermatoproteasome activity on sex chromosomes. There is evidence that HSF5 may in vivo form a complex with USP7 to reduce H2AK119ub on meiotic sex chromosomes. These results enhance our knowledge of HSF5's function during pachynema progression and shed fresh light on its intricate, multifaceted involvement in controlling important meiotic processes.

Keywords: transcriptional regulatory network, meiosis, XY body development, cell biology, molecular biology, and HSF5.

OVERVIEW

By reducing diploid cells to haploid gametes, the highly specialized cell division process known as meiosis ensures that genetic material is passed down across generations and encourages genetic variation through recombination. A single round of DNA replication initiates this complex process, which is followed by two separate division events (meiosis I and II) and ends with the creation of haploid cells (Zickler and Kleckner, 2015). Primary germ cells go through a protracted prophase I after the pre-meiotic S phase, during which time chromatin arrangement dynamically reorganizes. Programmed DNA double-strand breaks (DSBs) are introduced at leptotene to induce homologous recombination and facilitate DNA segment pairing. The axial element lengthens along the chromosome axis as homologous chromosomes align during the zygotene stage of meiosis, aiding in the creation of the synaptonemal complex, which mediates homolog pairing and recombination. After synapsis is finished, cells move into pachytene, where crossover recombination takes place. In the diplotene phase that follows, the synaptonemal complex disassembles asymmetrically. Until diakinesis, when chromosomes undergo additional compaction and bivalents separate from the nuclear membrane to start homolog segregation, and the process of meiosis. These include crucial checkpoints that are crucial for coordinating these processes, including the DNA damage checkpoint, synapsis checkpoint, and meiotic sex chromosome inactivation (MSCI) (Roeder and Bailis, 2000; Turner, 2015; Xie et al., 2022). Chromatin dynamically reorganizes during pachynema advancement, along with unique transcriptional and epigenetic alterations that together control meiotic progression (Rathke et al., 2014; Tahmasbpour Marzouni et al., 2022; Wang et al., 2024). The XY body, a structure essential to MSCI, is formed by the sequestration of the X and Y chromosomes inside a membraneless area inside the nucleus. Sex chromosomes are silenced as a result of MSCI, which is started when ATR phosphorylates H2AX, which in turn attracts MDC1 to γH2AX (Blanco-Rodríguez, 2009; Handel, 2020; Ichijima et al., 2011; Turner, 2015). Our knowledge of the order of these events has been improved by a recent study that suggested MSCI occurs before the XY body forms (Abe et al., 2020). Additionally, the formation of XY bodies is closely linked to a number of histone modifications, such as ubiquitination and methylation; liquid-liquid phase separation (LLPS) has recently been suggested as a possible mechanism underlying the formation and function of XY bodies (Alavattam et al., 2022; Page et al., 2012; Rao et al., 2017; Wu et al., 2020). These results imply that chromatin organization during pachynema is more intricate and multifaceted than previously thought, involving a mix of structural dynamics and metabolic changes. Significant changes in gene expression during prophase I have been documented in a number of studies. During the early phases (leptonema, zygonema, and early pachynema), transcriptional activity is minimal, but it resumes at the mid-pachytene (Green et al., 2018; Hong et al., 2022; Shima et al., 2004). As pachynema progresses, there is a noticeable change in gene expression, with meiosis-related genes significantly down-regulated and spermiogenesis-related genes up-regulated (Da Cruz et al., 2016; Guo et al., 2022). This change emphasizes how transcriptional reprogramming is dynamic and strictly controlled throughout this crucial stage of germ cell development. This intricate pattern of gene expression is orchestrated by the transcriptional regulatory network (TRN), which is essential for controlling meiotic progression and guaranteeing appropriate advancement through pachynema (Carrell, 2008; Hamazaki et al., 2021; Wang et al., 2024). The precise molecular processes controlling transcriptional regulation and chromatin remodeling in pachynema are still mostly unknown and need more research, despite tremendous advancements. According to our earlier research, heat shock factor 5 (HSF5),

belongs to the family of heat shock factors and plays a crucial role in regulating the transcription of genes necessary for the development of pachynema. HSF5 controls a wide range of transcriptional programs that coordinate both gene activation and repression by attaching to particular promoter regions (Luo et al., 2024). Interestingly, HSF5 suppresses genes including Sycp1, Meiob, Msh4, and Hat1, which results in a decrease in their transcriptional activity during important meiotic phases. On the other hand, HSF5 promotes the expression of genes such as Hspa2, Ccnb1, and Plk1 during the mid-to-late pachytene phase in order to become ready for the eventual transition to desynapsis (Luo et al., 2024). A severe meiotic arrest occurs at the mid-to-late pachytene stage when HSF5 is absent, leading to the

Pachytene spermatocytes are significantly reduced during prophase I. The fact that this happens in spite of typical synapsis, homologous chromosomal pairing, and MSCI-associated immunofluorescence (IF) signals suggests that HSF5's function goes beyond these mechanisms (Luo et al., 2024). In this work, we showed that HSF5 probably regulates the advancement of pachynema by controlling transcriptional reprogramming and chromatin dynamics. Notably, the TRN and global chromatin accessibility were disturbed in Hsf5−/− spermatocytes, and XY chromosome-associated activities, including spermatoproteasome activity, XY body formation, and epigenetic changes (including H2AK119ub and K48ub), displayed aberrant alteration.

SUPPLIES AND TECHNIQUES

Ethics declaration and mice

All mouse-related procedures were carried out in compliance with the Guide for the Care and Use of Laboratory Animals and were authorized by the Tab of Animal Experimental Ethical Inspection at Sir Run Run Shaw Hospital, Zhejiang University School of Medicine (approval no: SRRSH2025-0006). At Zhejiang University School of Medicine, mice were kept in a particular pathogen-free facility. Shanghai Model Organisms Center, Inc. (China) created the Hsf5−/− mouse model. In summary, a mMESSAGE mMACHINE T7 Ultra Kit (Ambion, USA) was used to transcribe Cas9 mRNA in vitro in accordance with the manufacturer's instructions. A MEGAshortscript Kit (Thermo Fisher, USA) was used to create two sgRNAs in vitro, one targeting Hsf5 intron 2 (5'-GCTGTATCTTACTTGGTTGA CGG-3') and the other targeting Hsf5 intron 3 (5'-AGTAGAAGCCAAAGATAGCT GGG-3'). After being microinjected into C57BL/6J mouse zygotes, Cas9 mRNA and sgRNAs were given to recipients who were not actually pregnant. Polymerase chain reaction (PCR) and sequencing were used to test the F0 offspring using the primer pair F-5'-AGCTCAAGAGGGAGGGAGAGAGAG-3' and R-5'-AGGCAGAGACATA GGGGAGCA-3'. To create F1 heterozygous Hsf5 knockout mice, positive F0 animals were bred with C57BL/6J mice. PCR was used to determine the F1 genotypes, and sequencing was used to confirm them. To create homozygous Hsf5−/− mice, male and female F1 heterozygous mice were crossed. Pachytene spermatocyte isolation .According to earlier studies, pachytene spermatocytes were separated by bovine serum albumin (BSA) gradient sedimentation (STA-PUT) (Luo et al., 2024). Following euthanasia, eight testes from four adult male mice (postnatal day 56, P56) were removed, decapsulated, rinsed in ice-cold phosphate-buffered saline (PBS) supplemented with 1× penicillin-streptomycin (Biochannel, BC-CE-007, China), and digested in Krebs-Ringer solution containing collagenase (0.5 mg/mL) at 33°C for 15 minutes in order to isolate seminiferous tubules. The tubules were resuspended in Krebs-Ringer solution with 0.5% BSA after being further digested for 10 minutes with trypsin (0.5 mg/mL) and DNase I (1 mg/mL). They were then passed through a 40 µm nylon cell strainer. Using the STA-PUT apparatus with a 2%–4% BSA gradient, the single-cell suspension was separated by unit-gravity sedimentation for three hours. Trypan blue exclusion was used to evaluate viability (Sunncell, SNK-004, China). Characteristic morphology (12–18 µm in diameter) and IF staining patterns with DAPI and γH2AX were used to identify pachytene spermatocytes. Pachytene cell-enriched fractions were combined for further examination.

Assay for transposase-accessible chromatin using high-throughput sequencing (ATAC-seq) preparation and sequencing of libraries

The Hyperactive ATAC-Seq Library Prep Kit for Illumina (Vazyme, TD711, China) was used to run ATAC-seq in accordance with the published workflow and manufacturer's instructions (Corces et al., 2017). The nuclei of about 5×105 STA-PUT-isolated pachytene spermatocytes were separated by centrifuging them at 500 ×g for 30 minutes at 4°C, resuspending them in 50 µL of cold lysis buffer, and then letting them sit on ice for 10 minutes. Following centrifugation, the nuclei were transposed for 30 minutes at 37°C in 50 µL of Tn5 transposase reaction mix. Stop buffer was used to halt the reaction for five minutes at room temperature. Indexing primers (Vazyme, TD202, China) were used to amplify adapter-ligated DNA fragments by PCR. VAHTS DNA Clean Beads (Vazyme, N411-01, China) were used to size-select the amplified DNA (200–800 bp), and a Qubit™4 Fluorometer (Invitrogen, USA) and Bioanalyzer 2100 (Agilent, USA) were used to measure the amount of DNA. Genedenovo Biotechnology (China) performed the sequencing of the libraries using the Illumina platform (USA).

Analysis of ATAC-seq data Fastp (v.0.23.4) was used to process raw reads for quality control (Chen, 2023), which included reducing low-quality bases and removing adapters. The mouse reference genome (mm39, Gencode, vM33) was aligned to quality-filtered reads using STAR (v.2.7.11b) with the following parameters: "--alignEndsType Local --outFilterMismatchNmax 10 --outFilterMultimapNmax 1 --alignMatesGapMax 700 The alignment of SJoverhangMin is 10. Read coverage and depth were computed using SAMtools (v.1.19.2) (Dobin et al., 2013; Li et al., 2009). Bedtools was used to filter PCR duplicate readings and reads that overlapped blacklist areas (Amemiya et al., 2019). After converting the filtered readings to BED format, MACS2 was used to call peaks with the following parameters: "-nomodel --shift -100 --extsize 200 -B --SPMR." DiffBind (v.3.16.0) (Ross-Innes et al., 2012) was used to identify differential ATAC-seq areas using absolute log2 fold change larger than 1 and false discovery rate (FDR) less than 0.01 as thresholds. Peak regions were then annotated using ChIPseeker (v.1.42.0) against the reference annotation dataset Gencode_vM33 (Wang et al., 2022). Using findMotifsGenome.pl in Homer (v.4.11) with default parameters, known motif finding inside peak regions was evaluated (Heinz et al., 2010). Furthermore, ATAC-seq signal track files in BigWig format were produced using the DeepTools (v.3.5.4) bamCoverage tool (Ramírez et al., 2016). The computeMatrix and plotHeatmap methods in DeepTools were used to create heatmaps of signals across all transcription start sites (TSSs) and peak summits.

Spreading spermatocytes with IF staining

The testes (P56 and P21) were fixed in Bouin's solution for frozen section IF, dried with various quantities of sucrose, and then embedded in Tissue-Tek OCT compound. Following antigen retrieval and three PBS washes, cryosections (5 µm) were placed onto slides. Following an overnight incubation with primary antibodies at 4°C in a humidified environment, the sections were cleaned and allowed to sit at room temperature for two hours before being incubated with secondary antibodies. When testes were dissected, seminiferous tubules were rinsed in order to observe spermatocyte spreading (Dia et al., 2017).

PBS and incubated for 45 minutes on ice in a hypotonic extraction buffer. After chopping the tubules in 100 mM sucrose and pipetting the germ cells out, they were placed on slides with 0.15% Triton X-100 and 1% paraformaldehyde (PFA) and incubated for the entire night at 4°C. Following the incubation period, the slides were cleaned with Photo-Flo 200, let to air dry, and then kept at -80°C.

The antibodies used for IF included: mouse anti-HSF5 (1:100, homemade), rat anti-H1t (1:100, homemade), rabbit anti-BRCA1 (1:100, homemade), rabbit anti-SYCP3 (1:200, Abcam, ab15093, UK), mouse anti-SYCP3 (1:200, Abcam, ab97672, UK), rabbit anti-γH2AX (1:200, Abcam, ab11174, UK), rabbit anti-MDC1 (1:200, Proteintech, 24721-1-AP, China), rabbit anti-SUMO1 (1:200, ABclonal, A19121, China), rabbit anti-SUMO2/3 (1:200, ABclonal, A22734, China), mouse anti-FK2 (1:200, Millipore, 4263, USA), mouse anti-E65C (1:200, Millipore, 05-678, USA), rabbit anti-H2AK119ub (1:200, Cell Signaling Technology, 8240, USA), rabbit anti- K48ub (1:200, Abmart, TC63005S, China), rabbit anti-PSMB2 (1:200, ABclonal, A13630, China), rabbit anti-PSMA7 (1:200, ABclonal, A4052, China), rabbit anti-RNF2 (1:200, ABclonal, A5563, China), rabbit anti-USP7 (1:200, ABclonal, A3448, China), rabbit anti-macroH2A.1 (1:200, ABclonal, A7045, China), rabbit anti-ATR (1:200, ABclonal, A22124, China), rabbit anti-H3K9me1 (1:100, ABclonal, A2358, China), rabbit anti-H3K9me2 (1:100, Affinity, DF6937, China), rabbit anti- H3K27ac (1:200, ABclonal, A7253, China), donkey anti-rabbit Alexa Fluor™ 488 (1:500, Thermo Fisher, A-21206, USA), donkey anti-mouse Alexa Fluor™ 555 (1:500, Thermo Fisher, A-31570, USA), and donkey anti-rat Alexa Fluor™ 647 (1:500, Thermo Fisher, A-48272, USA). A confocal fluorescence microscope (Zeiss, LSM980, Germany) was used to take photomicrographs.

Assays for proteasomes were conducted in 96-well plates with a 150 µL total volume. The reaction mixtures included 50 µg of protein supernatant extracted from STA-PUT-isolated spermatocytes in lysis buffer (20 mmol/L Tris-HCl (pH 7.4), 150 mmol/L NaCl, 1% Nonidet P-40, and 1 mmol/L EDTA), as well as 26S buffer (2 mmol/L ATP, 25 mmol/L HEPES, 0.5 mmol/L EDTA, and 0.01% SDS, pH 7.5). The mixtures were then incubated for 20 minutes at 37°C. To measure proteasome activities, fluorescently labeled substrates were added at a final concentration of 100 µmol/L: Z-Ala-Arg-Arg-AMC (ARR) for trypsin-like (β2), Suc-Leu-Leu-Val-Tyr-7-amino-4-methylcoumarin (LLVY) for chymotrypsin-like (β5), and Z-Leu-Leu-Glu-AMC (LLE) for caspase-like (β1) activities (MCE; HY-P1002, HY-134961, HY-123053; USA). Following the manufacturer's instructions, the Synergy H1 Multi-Mode Microplate Reader (Bio-Tek, USA) with 350 nm excitation and 440 nm emission was used to measure the release of free 7-amino-4-methylcoumarin (AMC) in 96-well plates (SAINING Biotechnology, AB2040320, China). The background signal was subtracted from the values obtained without protein after the data were standardized against it.

Histone extraction and analysis

In order to release their nuclei, purified pachytene spermatocytes (2×107) were resuspended in buffer A (250 mmol/L sucrose, 50 mmol/L KCl, 15 mmol/L NaCl, 10 mmol/L Tris-HCl (pH 7.4), 5 mmol/L MgCl2, 1 mmol/L CaCl2, 0.5% Triton X-100, 1 mmol/L DTT, 0.1 mmol/L PMSF, and 1× protease inhibitor) and incubated on ice for 10 minutes. Following centrifugation at 1,000 ×g for 10 minutes at 4°C, the pellet Triton X-100 was eliminated by washing with 1000 µL of buffer A, then 1000 µL of buffer B (10 mmol/L Tris-HCl (pH 7.4), 100 mmol/L NaCl, 5 mmol/L MgCl2, 10 mmol/L CaCl2, 300 mmol/L sucrose, 0.1 mmol/L PMSF, and 1×protease inhibitor). After resuspending the nuclei in 200 µL of buffer B and treating them with 5 µL with MNase (200 U/µL), they were shaken at 800 r/min for 20 minutes at 37°C. The pellet was resuspended in 100 µL of histone extraction buffer (20 mmol/L Tris-HCl (pH 7.9), 10 mmol/L EDTA, and 0.5 mol/L KCl) after centrifugation at 1 000 ×g for 10 min at 4°C. It was then kept on ice for 20 minutes and centrifuged at 16 000 ×g for 5 minutes at 4°C. Following protein quantification, Coomassie Brilliant Blue staining and 15% sodium dodecyl sulfate-polyacrylamide gel electrophoresis (SDS-PAGE) were used to 5 µg of histones.

With a few minor adjustments, transmission electron microscopy (TEM) was carried out as previously reported (Zhang et al., 2020). In summary, mouse testes (P70) were sliced into tiny pieces (about 2 mm long by 2 mm broad by 2 mm high) and preserved for at least 12 hours at 4°C in 0.1 mol/L phosphate buffer (PB, pH 7.4) that contained 4% PFA, 4% glutaraldehyde, and 0.2% picric acid. Samples were post-fixed with 1% OsO4, dehydrated, and infiltrated with a combination of acetone and Epon resin following three washes with 0.1 mol/L PB. After the samples were implanted and cut into 70 nm-thin slices, they were stained with lead citrate and uranyl acetate. A TEM operating at 100 kV (Tecnai Spirit, USA) was used to examine the ultrastructure.

Assay for in vivo ubiquitylation

Hsf5's coding sequence was cloned into pFLAG-CMV-4 (Tsingke Biotech, China). Co-transfection of HEK293T cells (Pricella Life Science & Technology, CL-0005, China) with 2 µg of pCMV6-HSF5-Flag and 2 µg of each of the following constructs was performed on 6-well plates (Jet Biofil, CAP011006, China): pCMV-HA-ubiquitin (WT), pCMV-HA-ubiquitin (K48), and pCMV-HA-ubiquitin (K48R). The cells were taken after 36 hours and lysed for 10 minutes on ice in 500 µL of lysis buffer (20 mM Tris-Cl (pH 7.4), 150 mmol/L NaCl, 1% NP-40, 0.25% SDC, 5% glycerol, 1 mmol/L DTT, and 1× protease inhibitor). Using the previously mentioned immunoprecipitation technique, ectopic HSF5 was immunoprecipitated from these lysates overnight at 4°C. Western blotting was used to examine the eluted proteins after the beads were cleaned with washing buffer and cooked in SDS sample buffer.

Western blotting (WB) and co-immunoprecipitation (Co-IP) were carried out using the Absin Co-IP Kit (Absin, abs9649, China), with a few minor adjustments. After homogenizing 1000 µL of lysis buffer (20 mmol/L Tris-Cl (pH 7.4), 150 mmol/L NaCl, 1% NP-40, 0.25% SDC, 5% glycerol, 1 mmol/L DTT, and 1 ×protease inhibitor), the STA-PUT-isolated spermatocytes (1×107) were centrifuged at 10 000 ×g for 10 minutes at 4°C. Protein A/G beads were used to precleave the supernatant, which was subsequently treated with primary antibodies for 4 hours at 4°C. High-salt Co-IP wash buffer (20 mmol/L Tris-Cl (pH 7.4), 300 mmol/L NaCl, 1% NP-40, 0.25% SDC, 5% glycerol, 1 mmol/L DTT, and 1× protease inhibitor) was used to wash the beads three times. 2× SDS gel-loading buffer was then used to elute the bound proteins from the beads. 500 µL of lysis buffer was used to generate lysates for plasmid-transfected cells (6-cm dishes), which were then treated as described above. Both inputs and outputs were separated using SDS-PAGE, moved to polyvinylidene fluoride (PVDF) membranes, blocked in PBST with 5% nonfat milk, treated with primary antibodies for an entire night at 4°C, washed three times with PBST, and then incubated with secondary antibodies conjugated with horseradish peroxidase (HRP). An Omni-ECLTM Femto Light Chemiluminescence Kit (Epizyme, SQ201, China) was used for protein detection, and the Bio-Rad ChemiDoc system was used for imaging. The following antibodies were used for Co-IP and WB: rabbit anti-HSF5 (1:1 000 for WB, 1:200 for Co-IP, homemade); rabbit anti-γH2AX (1:1 000, Abcam, ab11174, UK); rabbit anti-H1t (1:1 000, ABclonal, A18597, China); rabbit anti-macroH2A.1 (1:1 000, ABclonal, A7045, China); rabbit anti-USP7 (1:1 000 for WB, 1:200 for Co-IP, ABclonal, A3448, China); rabbit HA-tag (1:2 000, Bioworld, AP0005, USA); mouse FLAG-tag (1:2 000, Sino Biological, 109143-MM13, China); HRP-conjugated Affinipure goat anti-mouse IgG(H+L) (1:5 000, Proteintech, SA00001-1, China); and HRP-conjugated Affinipure goat anti-rabbit IgG (H+L) (1:5 000, Proteintech, SA00001-2, China).

Analysis of statistics

Every experiment was run at least three times on its own. Unless otherwise indicated, data in figures are displayed as mean±standard deviation (SD). GraphPad Prism v.10 was used for statistical analyses, and comparisons between experimental groups were carried out in accordance with the guidelines provided in the figure legends.

OUTCOMES

Chromosome accessibility landscape in Hsf5+/+ and Hsf5−/− pachytene spermatocytes

According to our earlier research, Hsf5 deletion modifies the transcriptional dynamics of genes that propel the evolution of pachynema and disturbs the transcriptome profiles of the disease (Luo et al., 2024). In order to determine if this dysregulation is due to changes in chromatin accessibility, the genomic chromatin

accessibility landscapes of Hsf5+/+ and Hsf5−/− pachytene spermatocytes were compared using ATAC-seq. For ATAC-seq, high-purity pachytene spermatocytes (about 78%) were initially extracted from P56 testes using STA-PUT (Supplementary Figure S1A–C). Strong concordance was shown by two separate biological replicates, indicating that they were appropriate for data integration (Supplementary Figure S1D).
Figure 1A shows that MACS2 identified 64 111 peaks in Hsf5−/− and 37 025 peaks in Hsf5+/+. Peak annotations in Hsf5+/+ were primarily enriched at untranslated regions (UTRs) (1.06%), exons (3.07%), introns (13.34%), intergenic regions (25.04%), and promoters (−3 000 bp to +3 000 bp of TSSs, 57.5%) (Supplementary Figure S1E). Peaks in Hsf5−/− were concentrated in intergenic areas (27.08%), exons (4.74%), introns (16.68%), UTRs (1.8%), and promoters (49.71%) (Supplementary Figure S1F). The majority of peaks showed notable chromosomal overlap with gene TSSs (Supplementary Figure S1G), which is in line with the ATAC signal's enrichment at TSSs during spermatogenesis (Maezawa et al., 2018). Global accessibility rose in Hsf5−/− compared to Hsf5+/+ (35 050 locations gained accessibility and 925 regions lost accessibility; FDR<0.05 and fold change≥1) (Figure 1A; Supplementary Figure S1H), despite generally similar genomic patterns (Supplementary Figure S1E–G).

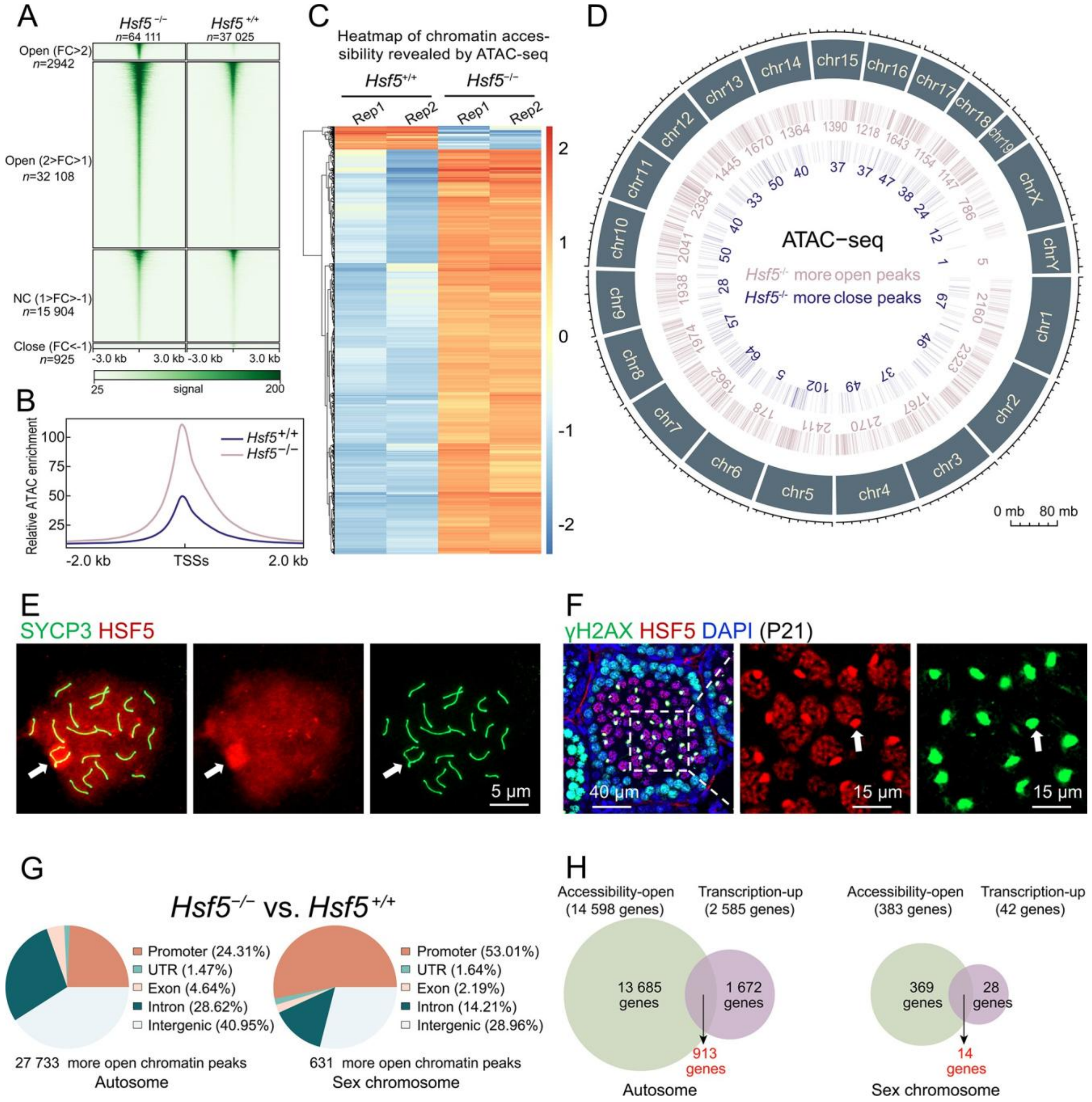

Figure 1 Chromatin accessibility and multi-omics analysis of *Hsf5*$^{+/+}$ and *Hsf5*$^{-/-}$ pachytene spermatocytes

A: Heatmap showing ATAC peaks based on changes in *Hsf5*$^{-/-}$ and *Hsf5*$^{+/+}$ pachytene cells. Each row represents a locus; green gradient indicates ATAC-seq signal intensity. B: Metaplot showing ATAC-seq signals at TSSs in *Hsf5*$^{+/+}$ and *Hsf5*$^{-/-}$ cells. C: Heatmap of two independent ATAC-seq analyses based on normalized log$_2$(RPM) values of *Hsf5*$^{+/+}$ and *Hsf5*$^{-/-}$ cells. Total number of differentially accessible ATAC peaks in *Hsf5*$^{-/-}$ cells was 35 975, with 35 050 being more open and 925 being more closed. D: Distribution of 35 975 differentially accessible peaks across chromosomes. E: HSF5 staining with SYCP3 on chromosome spreads of pachytene spermatocytes from adult *Hsf5*$^{+/+}$ testes. Arrow indicates XY body. Scale bars are shown. F: γH2AX staining with HSF5 on testis sections at P21. Right two panels show magnifications of boxed areas in the left panel. Arrow indicates XY body. Scale bars are shown. G: Distributions of more open ATAC-seq peaks on autosomes and sex chromosomes in *Hsf5*$^{-/-}$ vs. *Hsf5*$^{+/+}$ pachytene cells. Two sets of data were normalized and combined for analysis. H: Venn diagrams of up-regulated genes from scRNA-seq (pachytene) data and genes with more open ATAC peaks.

pronounced increase at TSSs (Figure 1B). Heatmaps of normalized signal (reads per million mapped reads, RPM) centered on peaks corroborated widespread accessibility gains (Figure 1C). Differentially accessible peaks (35 975 total) were evenly distributed across chromosomes without detectable chromosomal bias (Figure 1D). Taken together, these results indicate that *Hsf5* deletion alters overall chromatin accessibility in spermatocytes, leading to agenerally more open chromatin structure, particularly at TSSs, although a minority of loci exhibited reduced accessibility.

Multi-omics data integration reveals distinct regulation of chromatin accessibility and transcription on autosomes and sex chromosomes by HSF5

Given the distinct chromatin accessibility characteristics of autosomes and sex chromosomes in spermatocytes (Maezawa et al., 2018) and the marked enrichment of HSF5 on the XY chromosomes (Figure 1E, F), newly accessible peaks in *Hsf5*$^{-/-}$ were stratified by chromosome class and analyzed separately for autosomes and XY chromosomes. As shown in Figure 1G, compared with *Hsf5*$^{+/+}$ pachytene cells, autosomes in *Hsf5*$^{-/-}$ pachytene cells exhibited 27 733 open chromatin peaks, whereas the XY chromosomes contained 631 open chromatin peaks. Notably, open peaks on the sex chromosomes were substantially more enriched in promoter regions, accounting for 53.01% compared with only 24.31% enrichment on autosomes (Figure 1G). These data indicate a genome-wide increase in chromatin accessibility across autosomes and the XY chromosomes, with promoter regions on the sex chromosomes showing a disproportionate gain in *Hsf5*$^{-/-}$ pachytene cells relative to *Hsf5*$^{+/+}$.

To determine whether accessibility changes were associated with the transcriptional expression of corresponding genes, previously generated 10x Genomics single-cell RNA-seq (scRNA-seq) data (Luo et al., 2024) were integrated with ATAC-seq. In *Hsf5*$^{+/+}$, early (eP), middle (mP), and late pachytene (lP) clusters were merged into a single pachytene group, while in *Hsf5*$^{-/-}$, the eP and pachytene-like clusters were merged. Differentially expressed genes (DEGs) were defined using adjusted $P<0.01$ and $|\text{fold change}|>1$, yielding 2 627 up-regulated genes (2 585 autosomal and 42 XY-linked) and 3 013 down-regulated genes (2 944 autosomal and 64 XY-linked) (Supplementary Table S1). Expression shifts for autosomal and XY-linked genes were broadly similar between genotypes (Supplementary Figure S2A, B), consistent with IF staining for Pol II, H3K9ac, and H3K9me3 and with qPCR results, which detected no overt abnormalities between *Hsf5*$^{-/-}$ and *Hsf5*$^{+/+}$ (Luo et al., 2024). Further analysis indicated that 35.3% (913/2 585) of up-regulated autosomal genes and 23.8% (10/42) of up-regulated XY-linked genes were associated with one or more open chromatin regions (Figure 1H), suggesting that the altered chromatin accessibility patterns in *Hsf5*$^{-/-}$ pachytene spermatocytes were weakly coupled to transcriptional activation. Specifically, although chromatins were more open in the absence of HSF5, the transcription of these genes did not increase accordingly. Notably, our findings, which show no strong correlation between chromatin accessibility and gene transcription in *Hsf5*$^{-/-}$, align with previous studies. For instance, (Maezawa et al., 2018) observed that, despite transcriptional silencing associated with MSCI, a substantial number of unique ATAC peaks appeared on the sex chromosomes. Similarly, (Miyamoto et al., 2018) emphasized that chromatin accessibility does not always correlate with transcriptional activity in oocytes. Furthermore, during the mid-pachytene stage, XY chromosomes do not exhibit DAPI-dense heterochromatin characteristics in cytological analyses (Supplementary Figure S2C), suggesting that transcriptional silencing of the XY chromosomes may not be linked to chromatin compaction, a finding also reported by (Alavattam et al., 2022).

TRN is altered in *Hsf5*$^{-/-}$ pachytene spermatocytes Transcriptional reprogramming governed by the TRN plays a crucial role in ensuring the proper progression of pachynema and predicts both target gene expression and downstream biological processes (Carrell, 2008). Based on scRNA-seq data (eP, mP, and lP) and the TRRUST v2 database (Han et al., 2018; Luo et al., 2015), 190 transcription factors (TFs) involved in pachynema progression were identified, including *Hnrnpk*, *Ezh1*, *Hsf1*, and *Yy1* (Figure 2A). Because *Hsf5*$^{-/-}$ testes did not progress to lP (Luo et al., 2024), analyses focused on target downstream genes (TDGs) regulated by eP- and mP-enriched TFs that normally drive advancement to lP. Across these TFs, 1 092 TDGs were identified and classified as activated, repressed, or unknown based on regulation by upstream TFs (Figure 2B). Compared with *Hsf5*$^{+/+}$, *Hsf5*$^{-/-}$ pachytene cells exhibited two distinct TDG sets with marked changes: 108 down-regulated and 179 up-regulated genes, including meiotic regulators such as *Cdk1*, *Tcfl5*, and *Uhrf1* (Clement et al., 2015; Dong et al., 2019; Galán-Martínez et al., 2022). Based on Gene Ontology (GO) enrichment analysis, the 108 down-regulated TDGs were enriched in “negative regulation of apoptotic process”, “cell division”, and “chromatin remodeling”, while the 179 up-regulated TDGs were enriched in “chromatin remodeling”, “apoptotic process”, and “protein phosphorylation”. TRRUST v2 analysis showed that expression shifts tracked the annotated regulatory direction of upstream transcription factors. In the down-regulated TDG set, 39.8% (43/108) were annotated as repressed by their regulators, exceeding the 16.7% (18/108) annotated as activated. In the up-regulated set, 37.9% (68/179) were annotated as activated, nearly threefold the 12.8% (23/179) annotated as repressed. These distributions indicate that core transcription factor programs and the associated TRN coordinate pachynema progression, and that loss of HSF5 triggers network-wide dysregulation culminating in pachytene arrest.

Because accessible chromatin frequently harbors TF- binding sites (Buenrostro et al., 2013), the identified TFs were integrated with ATAC-seq profiles. Motif analysis with HOMER on regions that gained accessibility in *Hsf5*$^{-/-}$ identified a group of consensus motifs matching known sites in pachytene spermatocytes. The inferred regulators included factors essential for spermatogenesis, including nuclear factor Y (NFYA and NFYB) and members of the SOX and POU families (Hou et al., 2012; Wu et al., 2010). HOMER motif analysis identified TF families also highlighted in Figure 2A (SP, SOX, KIF, TCF; Figure 2C), and the targets of these factors overlapped meiosis-related TDGs in Figure 2B (e.g., *Ccnb1*, *Bsg*, *Setdb1*; Figure 2D), collectively indicating a remodeled transcriptional regulatory network in *Hsf5*$^{-/-}$ pachytene spermatocytes.

XY body formation and histone composition are altered in *Hsf5*$^{-/-}$ pachytene spermatocytes

To assess whether altered chromatin accessibility and TRN disruption were associated with changes in nucleosome composition and XY body formation in *Hsf5*$^{-/-}$ pachytene spermatocytes, nucleosomes were purified from *Hsf5*$^{+/+}$ and *Hsf5*$^{-/-}$ pachytene cells and the abundance of canonical histones and variants was quantified by Coomassie Brilliant Blue staining. Core histones H3 and H4 were comparable between genotypes (Figure 3A, black arrows), whereas H2 was reduced in *Hsf5*$^{-/-}$ nucleosomes (Figure 3A, red arrows, lower red asterisk). Histone H1 isoforms, reported to range from 25 to 35 kDa (Lin et al., 2024; Shechter et al., 2007), also displayed three bands in *Hsf5*$^{+/+}$ pachytene cells, whereas only two higher-molecular-mass bands were observed in *Hsf5*$^{-/-}$ pachytene cells (Figure 3A, blue arrows, upper red asterisk). Immunoblotting of whole-cell extracts corroborated these trends, revealing decreased H1t, γH2AX (Ser139-phosphorylated H2AX), and macroH2A.1 in *Hsf5*$^{-/-}$ pachytene

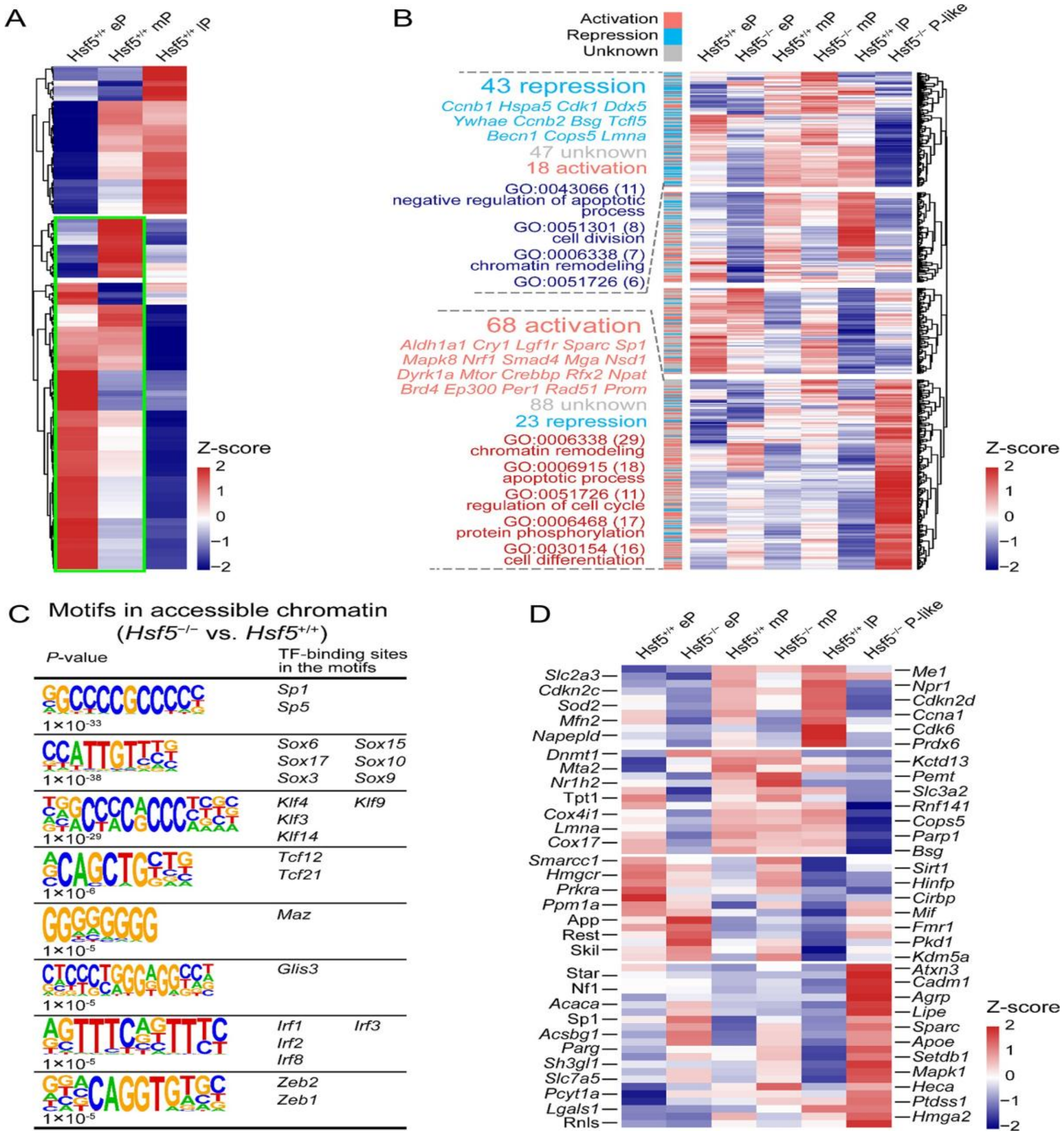

Figure 2 TRN alterations in *Hsf5*$^{-/-}$ pachytene spermatocytes

A: Heatmap showing TF expression patterns in spermatocytes during *Hsf5*$^{+/+}$ pachynema progression. Each row represents a gene; each column represents a single cell. B: Heatmap showing TDGs regulated by TFs (highlighted in green box in A) in *Hsf5*$^{+/+}$ and *Hsf5*$^{-/-}$ pachytene cells during pachynema. Each row represents a gene; each column represents a single cell. Leftmost column indicates regulatory annotation for each TDG (activated, repressed, unknown). C: HOMER motif enrichment of regions with increased ATAC-seq accessibility in *Hsf5*$^{-/-}$ pachytene cells, identifying putative TF-binding sites that overlap with factors in A. D: Heatmap showing expression patterns of TDGs regulated by TFs in C in *Hsf5*$^{+/+}$ and *Hsf5*$^{-/-}$ pachytene cells during pachytene. Each row represents a gene; each column represents a single cell.

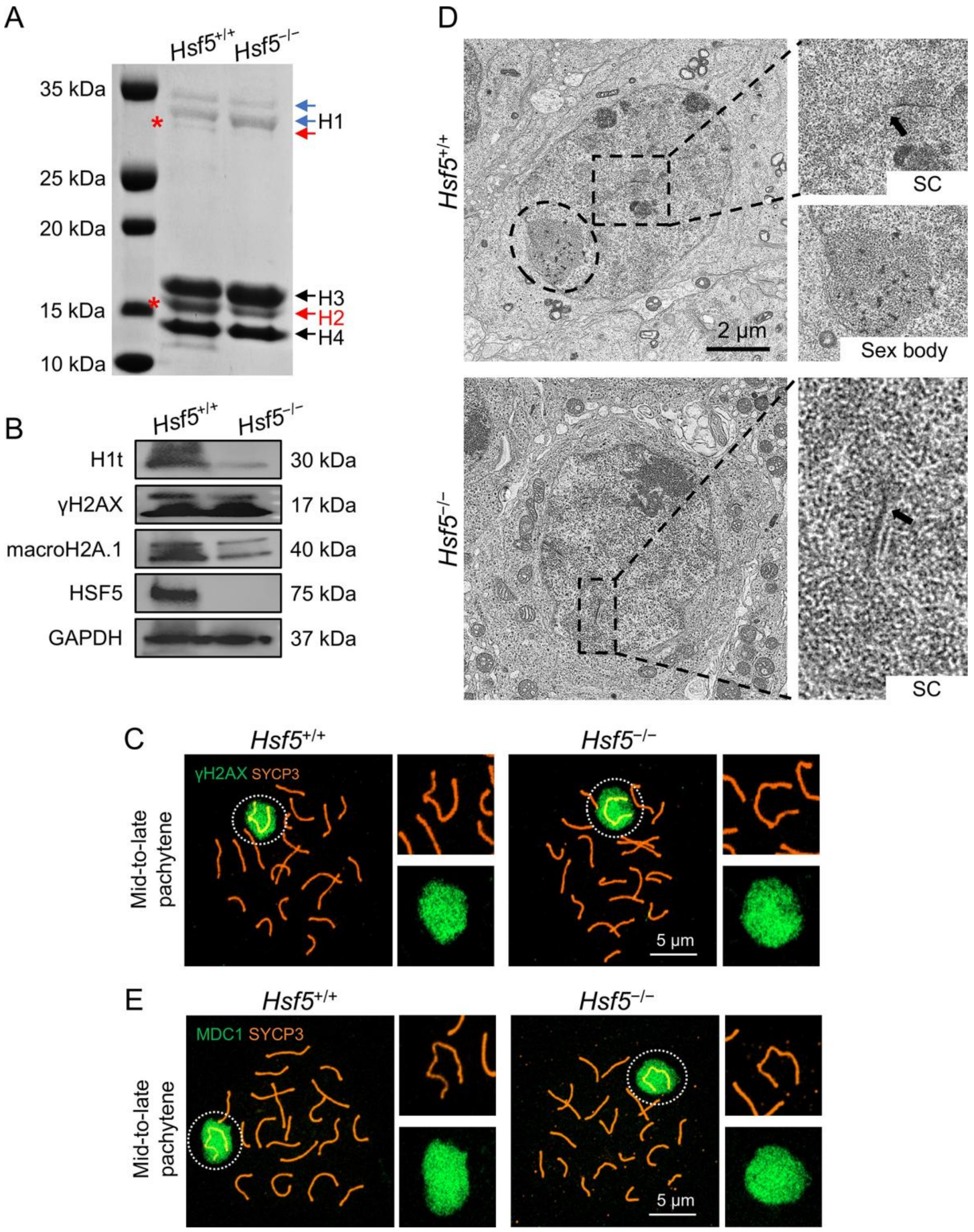

Figure 3 Nucleosome composition, TEM analysis, and γH2AX-MDC1 signaling pathway in *Hsf5*$^{+/+}$ and *Hsf5*$^{-/-}$ pachytene spermatocytes

A: Coomassie Brilliant Blue staining of purified nucleosomes from *Hsf5*$^{+/+}$ and *Hsf5*$^{-/-}$ pachytene cells. Red asterisks indicate altered histones. B: WB analysis of histone variants (H1t, γH2AX, and macroH2A.1) in *Hsf5*$^{+/+}$ and *Hsf5*$^{-/-}$ pachytene cells. GAPDH, loading control. C: SYCP3 was co-stained with γH2AX on chromosome spreads from P56 *Hsf5*$^{+/+}$ and *Hsf5*$^{-/-}$ mice. Dashed circles indicate sex chromosome area. Scale bar is shown. D: TEM images of representative pachytene spermatocytes in *Hsf5*$^{+/+}$ and *Hsf5*$^{-/-}$ mice. XY body (black dashed oval) and synaptonemal complex (SC, black dashed box) were observed in *Hsf5*$^{+/+}$ pachytene spermatocytes. XY body appeared as a round, lighter, and more homogeneous mass compared with other areas in the cell nucleus. In contrast, no distinct XY body was observed in *Hsf5*$^{-/-}$ pachytene spermatocytes, although SC (arrowhead) was still visible. Scale bar is shown. E: SYCP3 was co-stained with MDC1 on chromosome spreads from P56 *Hsf5*$^{+/+}$ and *Hsf5*$^{-/-}$ mice. Dashed circles indicate sex chromosome area. Scale bar is shown.spermatocytes (Figure 3B). In contrast, nuclear spread IF detected similar H1t, γH2AX, and macroH2A.1 signals in both genotypes (Figure 3C; Supplementary Figure S3A, B). These observations indicate a role for HSF5 in establishing normalcore and linker histone composition in pachytene spermatocytes. However, due to pachynema progression arrest, these changes could also be attributed to a biased distribution of meiotic substages in *Hsf5*$^{-/-}$ pachytene cells

Supplementary Figure S3C).

Next, TEM was used to analyze nuclear ultrastructure and chromosome behavior. Synaptonemal complexes, formed between homologous autosomes and characterized by extruding condensed chromatin fibers, were evident in both *Hsf5*$^{+/+}$ and *Hsf5*$^{-/-}$ pachytene spermatocytes. In *Hsf5*$^{+/+}$ testes, the XY chromatin formed a characteristic XY body—an elliptical, lightly stained, homogeneous domain—observed in 58.7% (128/218) of cells (Figure 3D, black arrow). In adult *Hsf5*$^{-/-}$ testes, XY bodies were rare, present in only 5.9% (16/270) of sections showing XY body-like structures. Recruitment of DNA damage response (DDR) proteins to the sex chromosomes precedes XY body formation (Alavattam et al., 2022). Consistent with this sequence, γH2AX, MDC1, ATR, and BRCA1, core components of the DDR pathway, exhibited normal localization in both genotypes (Figure 3C, E; Supplementary Figure S3D, E). Together, these findings place HSF5 downstream of the γH2AX-MDC1 signaling pathway on meiotic sex chromosomes and indicate that HSF5 is required for proper compartmentalization of X and Y chromosomes into the XY body domain.

Defective epigenetic programming of meiotic sex chromosomes in the absence of HSF5

Meiotic sex chromosomes undergo extensive epigenetic reprogramming downstream of the γH2AX-MDC1 signaling pathway. Furthermore, because ubiquitin and SUMO modifications exhibit dynamic patterns during prophase I and regulate multiple meiotic processes in mice (Alavattam et al., 2022; Rao et al., 2017), SUMOylation and ubiquitylation were examined on sex chromosomes in *Hsf5*$^{-/-}$ pachytene spermatocytes. Signals detected with anti-SUMO1 and anti- SUMO2/3 antibodies accumulated at centromeric heterochromatin and across XY chromatin in pachynema, with no detectable differences between genotypes (Figure 4A, B). As ubiquitin modification regulatory impact depends on chain type (monoubiquitin or polyubiquitin) (Hasegawa et al., 2015), antibody clone E65C was used to detect RNF8-mediated H2A polyubiquitination, and clone FK2 was used to detect monoubiquitin and K29-, K48-, and K63-linked polyubiquitin chains (Hasegawa et al., 2015). At mid-to-late pachytene, FK2 and E65C signals were robust and encompassed the XY body in *Hsf5*$^{+/+}$ spermatocytes, with comparable patterns in *Hsf5*$^{-/-}$ spermatocytes (Figure 4C, D).

H2A monoubiquitination (H2AK119ub) and K48-linked ubiquitination (K48ub), two ubiquitin marks associated with meiotic regulation (Hasegawa et al., 2015; Luo et al., 2015; Rao et al., 2017), were profiled. In *Hsf5*$^{+/+}$ pachytene spermatocytes, H2AK119ub was not enriched within the XY body (Figure 4E), consistent with prior observations (Hasegawa et al., 2015). However, in *Hsf5*$^{-/-}$ pachytene spermatocytes, H2AK119ub was significantly up-regulated on the XY pair, with similar signals observed on autosomes compared with *Hsf5*$^{+/+}$ cells (Figure 4E). K48ub, which targets proteins for degradation via the ubiquitin-proteasome system

(Rao et al., 2017), displayed diffuse nuclear distribution in *Hsf5*$^{+/+}$ pachytene cells (Figure 4F). Notably, K48ub signals were relatively reduced on the XY pair, with no obvious autosomal abnormalities (Figure 4F). These results suggest that HSF5 is differentially involved in the ubiquitin modification of XY chromosomes and autosomes, and that HSF5 deficiency may disrupt H2AK119ub and K48ub regulation on meiotic sex chromosomes.To determine whether HSF5 deficiency and abnormal ubiquitination (H2AK119ub and K48ub) affected the distribution of other epigenetic modifications downstream of the γH2AX-MDC1 signaling pathway on meiotic sex chromosomes, additional histone marks were examined. In *Hsf5*$^{-/-}$ pachytene spermatocytes, the mono- and dimethylation of H3K9 (H3K9me1 and H3K9me2), as well as histone H3 acetylation at lysine 27 (H3K27ac), remained unchanged compared with *Hsf5*$^{+/+}$ cells (Supplementary Figure S4A–C). These data suggest that HSF5 participates in the regulation of ubiquitination of XY chromosomes, and disordered ubiquitination on XY chromosomes likely leads to the pachytene arrest and apoptotic cell death observed in *Hsf5*$^{-/-}$ spermatocytes (Luo et al., 2024).

***Hsf5*-deficient spermatocytes exhibit abnormal spermatoproteasome signals on meiotic sex chromosomes**

Reduced K48ub-linked ubiquitin on XY chromosomes, together with the role of K48ub chains in targeting proteins for degradation via the ubiquitin-proteasome system (Rao et al., 2017), termed the spermatoproteasome during spermatogenesis (Gómez et al., 2019), prompted examination of spermatoproteasome localization and activity in *Hsf5*$^{-/-}$ spermatocytes. Immunostaining for PSMB2 (β-type) and PSMA7 (α-type) subunits of the cylindrical catalytic core particle in proteasome complexes (Collins and Goldberg, 2017) revealed axis-associated signals that colocalized with SYCP3 on both sex chromosomes and autosomes in *Hsf5*$^{+/+}$ pachytene spermatocytes (Figure 4G, H). However, in *Hsf5*$^{-/-}$ spermatocytes, these signals were absent from the XY chromosomes, while similar signals were observed on autosomes compared with *Hsf5*$^{+/+}$ cells (Figure 4G, H). Proteasomal catalytic output in whole-cell extracts from pachytene spermatocytes was quantified by measuring chymotrypsin-like activity (associated with the β5 catalytic subunit), caspase-like activity (β1), and trypsin-like activity (β2) (Gomes et al., 2009). Biochemical analysis revealed comparable proteasomal activity in *Hsf5*$^{-/-}$ and *Hsf5*$^{+/+}$ extracts (Figure 4I). However, this equivalence does not exclude XY- specific alterations, as the presence of autosome-associated proteasomes could mask potential differences.

HSF5 functions as an E3 ligase or as a ubiquitination substrate

To test whether HSF5 functions as an E3 ligase or serves as a substrate for ubiquitination, HEK293T cells were co- transfected with pCMV6-HSF5-Flag and various expression plasmids: pCMV-HA-ubiquitin (wild-type, WT), pCMV-HA- ubiquitin (K48), in which all lysine residues, except for lysine at position 48, were mutated to arginine, and pCMV-HA-ubiquitin (K48R), where the lysine at position 48 was substituted with arginine. Cells were harvested 36 h after transfection for protein extraction. Whole-cell extracts (WCE) were immunoprecipitated using an anti-FLAG antibody to enrich HSF5 and its potential interacting partners. The WCE and immunoprecipitation eluates were then analyzed by WB for HA-ubiquitin detection. Co-expression of pCMV6-HSF5-Flag with HA-ubiquitin variants (WT, K48-only, K48R) generated HA-reactive ubiquitin conjugates across a broad molecular-weight range, whereas extracts lacking HA-ubiquitin or expressing HSF5 alone showed little or no signal (Figure 4J). Anti-FLAG immunoprecipitation enriched HA-ubiquitin in association with ectopic HSF5, while the pCMV6-HSF5-Flag-

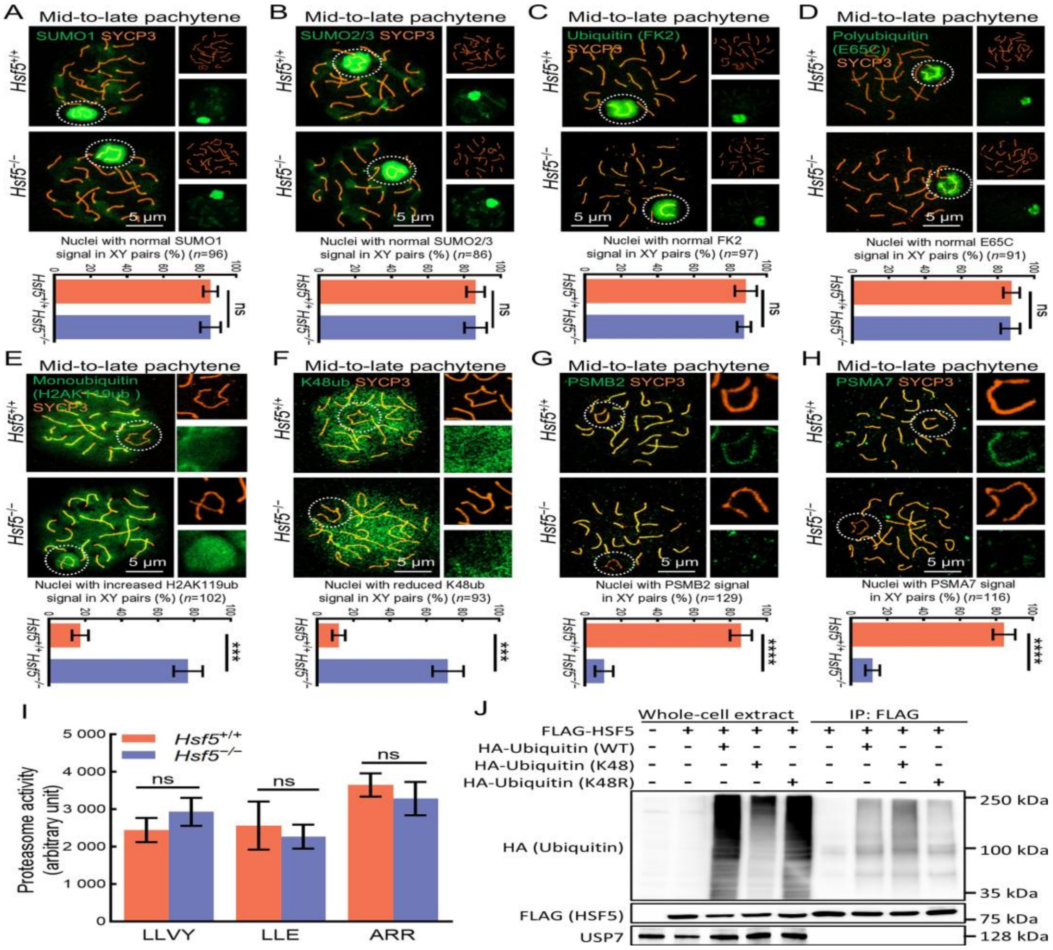

Figure 4 Epigenetic programming and spermatoproteasome signal analysis of meiotic sex chromosomes in *Hsf5*$^{-/-}$ pachytene spermatocytes

A–H: SYCP3 was co-stained with SUMO1, SUMO2/3, FK2, E65C, H2AK119ub, K48ub, PSMB2, and PSMA7 on chromosome spreads from P56 *Hsf5*$^{+/+}$ and *Hsf5*$^{-/-}$ mice. Dashed circles indicate sex chromosome area. Scale bars are shown. Three males were used in each experiment*;* *n*, number of pachytene spermatocytes analyzed. Data are presented as mean±SD; ns: Not significant; ***: $P<0.001$; ****: $P<0.0001$ (Mann-Whitney U test). I: Proteasome activity of *Hsf5*$^{+/+}$ and *Hsf5*$^{-/-}$ pachytene spermatocytes. Fluorescently labeled substrates LLVY, LLE, and ARR were used to detect chymotrypsin-like (β5 catalytic subunit), caspase-like (β1 catalytic subunit), and trypsin-like (β2 catalytic subunit) activities, respectively. Data were normalized to the background signal, with values obtained without protein subtracted for correction; ns: Not significant (two-way ANOVA). J: *In vivo* ubiquitylation assay showing substantial HA-tagged ubiquitin in association with ectopic HSF5 protein.only control yielded minimal HA signal (Figure 4J). These findings indicate that HSF5 either catalyzes ubiquitin transfer or serves as a ubiquitination substrate, and that chain types are not restricted to K48 linkages.HSF5-USP7 complex suppresses H2AK119ub on meiotic sex chromosomes *in vivo*

To investigate the basis for elevated H2AK119ub on meiotic sex chromosomes, enzymes mediating ubiquitination and

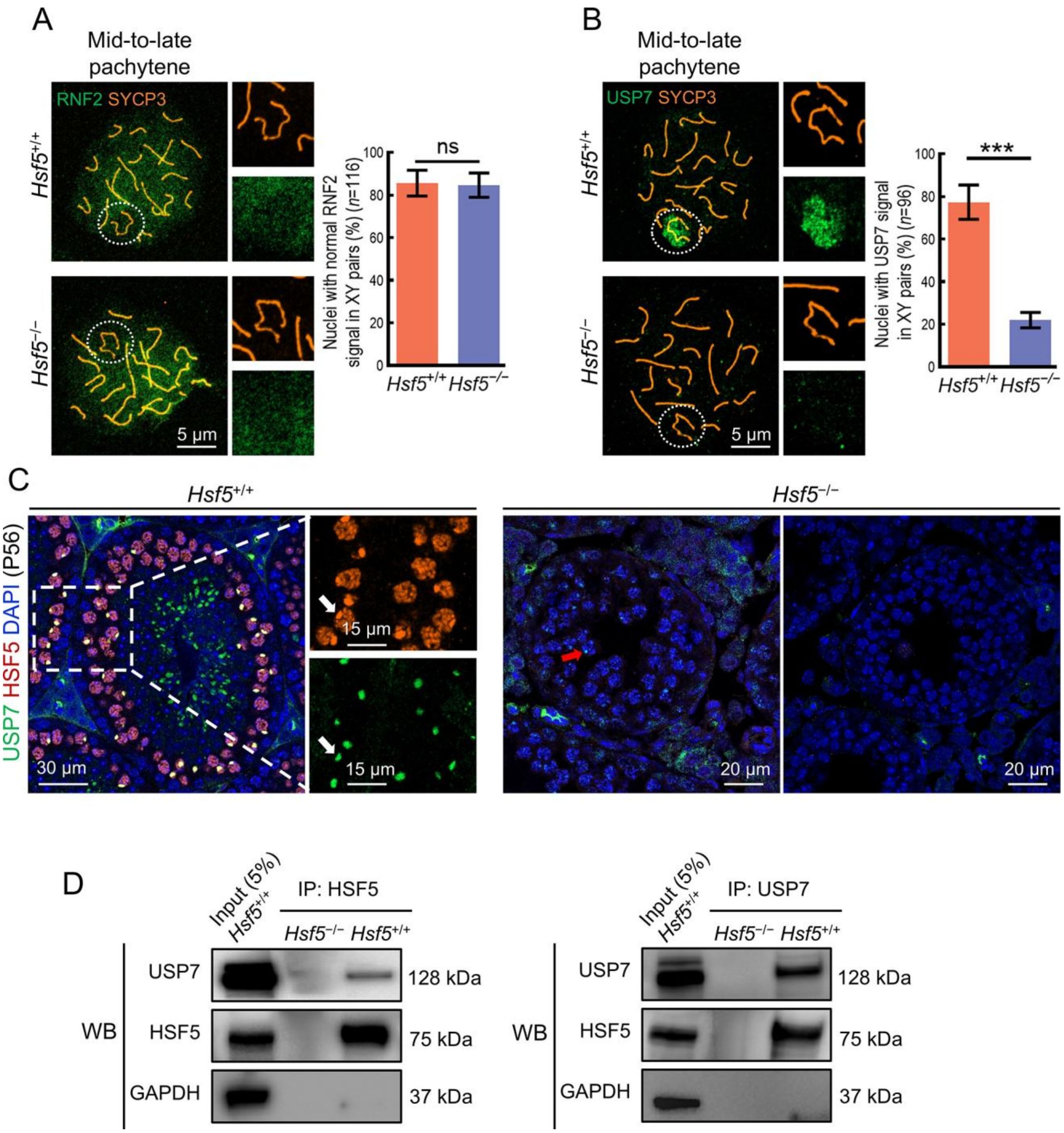

Figure 5 HSF5-USP7 complex suppresses H2AK119ub on meiotic sex chromosomes *in vivo*

A, B: SYCP3 was co-stained with RNF2 and USP7 on chromosome spreads from P56 *Hsf5*$^{+/+}$ and *Hsf5*$^{-/-}$ mice. Dashed circles indicate sex chromosome area. Scale bars are shown. Three males were used in each experiment; *n*, number of pachytene spermatocytes analyzed. Data are presented as mean±SD; ns: Not significant; ***: *P*<0.001 (Mann-Whitney *U* test). C: USP7 was co-stained with HSF5 on testis sections from P56 *Hsf5*$^{+/+}$ and *Hsf5*$^{-/-}$ mice. Gray arrow indicates XY body, where HSF5 and USP7 were highly enriched and colocalized in *Hsf5*$^{+/+}$ cells. In contrast, USP7 signals were absent or weak in *Hsf5*$^{-/-}$ cells, as indicated by red arrow. Scale bars are shown. D: Co-IP of HSF5 with USP7 in *Hsf5*$^{+/+}$ pachytene spermatocytes. GAPDH, loading control.

rabbit anti-HSF5 and anti-USP7 antibodies confirmed an association between HSF5 and USP7 in *Hsf5*$^{+/+}$ but not *Hsf5*$^{-/-}$ samples (Figure 5D). This interaction was not detectable after HSF5 overexpression from pCMV6-HSF5-Flag in cultured cells (Figure 4J). These data support formation of an endogenous HSF5-USP7 complex on meiotic sex chromosomes in vivo that likely constrains H2AK119ub on the XY pair.

In summary, integrated multi-omics and cell biology analyses revealed an indispensable role of HSF5 for proper chromatin behavior and transcriptional reprogramming to drive pachynema progression (Figure 6). Loss of *Hsf5* leads to a more open chromatin state, triggering a cascade of abnormal TRN responses, defective XY body formation, altered histone composition, decreased XY-linked K48ub and spermatoproteasome signals, and increased H2AK119ub on XY chromatin, ultimately resulting in pachytene arrest. The evidence supports a dual role for HSF5 during pachynema progression, acting either as an E3 ligase or ubiquitination substrate on XY chromatin, or interacting with USP7 to suppress XY-linked H2AK119ub.

DISCUSSION

Meiosis is critical for the production of gametes, ensuring genetic diversity and the proper segregation of chromosomes. In this study, testis-specific protein HSF5 was identified as essential for the coordination of chromatin dynamics and transcriptional reprogramming during pachynema progression. Integrated multi-omics and cell biology analyses delineatedhow HSF5 shapes accessibility landscapes, histone composition, XY body architecture, and ubiquitin-based signaling on sex chromosomes.

ATAC-seq revealed widespread remodeling of chromatin accessibility after *Hsf5* deletion, with a global increase in open chromatin regions, particularly at TSSs. These shifts may impact the binding of TFs and other regulatory proteins, ultimately disrupting the TRN. Concordant changes in histone composition and abnormal XY body formation in *Hsf5*$^{-/-}$ pachytene spermatocytes further implicate HSF5 in chromatin remodeling during pachynema, as reported in previous studies. Notably, while proper XY body formation was not observed in *Hsf5*$^{-/-}$ pachytene spermatocytes, normal γH2AX and MDC1 signals were detected on the sex chromosomes, suggesting that DDR-directed meiotic silencing in early MSCI precedes HSF5-mediated XY body formation (although DDR-directed silencing does not always coincide with XY body formation). Loss of HSF5 also led to abnormal ubiquitination patterns on meiotic sex chromosomes, characterized by increased H2AK119ub and decreased K48ub signals on the XY chromosomes, suggesting that HSF5 differentially regulates ubiquitin modification on XY chromosomes and autosomes. Mechanistically, the data support a model in which HSF5 either participates directly in ubiquitination on XY chromatin (as an E3 ligase or as a substrate) and/or cooperates with USP7 to restrain H2AK119ub, thereby maintaining an epigenetic environment permissive for pachynema progression.

Several questions remain to be answered. First, current TF

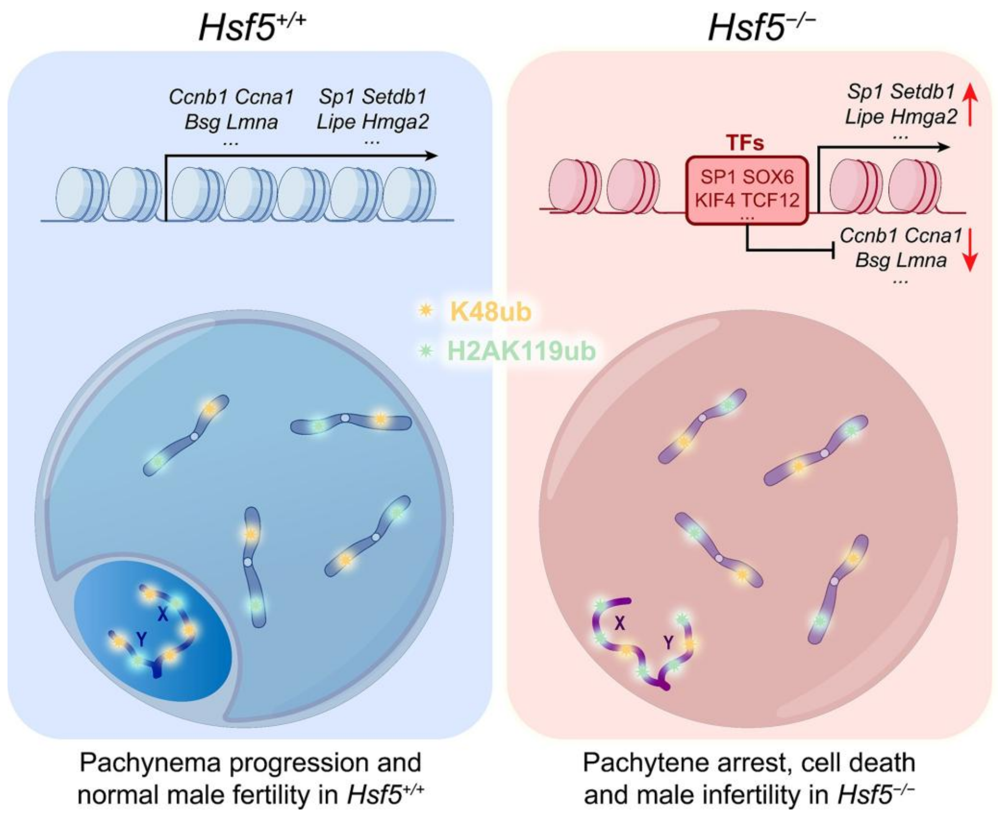

Figure 6 Pachytene development in fertile mice vs. pachytene arrest in *Hsf5*$^{-/-}$ infertile mice

Deletion of *Hsf5* leads to altered histone composition and a more open chromatin state, with TFs such as the SP, SOX, KIF, and TCF families being abnormally enriched, triggering a cascade of aberrant TRN responses, including down-regulation of genes such as *Ccnb1*, *Ccna1*, *Bsg*, and *Lmna*, and up-regulation of genes such as *Sp1*, *Setdb1*, *Lipe*, and *Hmga2*. Additionally, deletion of *Hsf5* leads to defective XY body formation, decreased XY-linked K48ub, and increased H2AK119ub on XY chromatin, ultimately resulting in pachytene arrest.TF-target maps and repositories are not comprehensive. Notably, the regulation of many TDGs is still unclear, and many genes cannot yet be attributed to upstream TFs. For instance, integrated study of the TRRUST v2 database and HOMER failed to identify HSPA2, SYCP1, and MEIOB, which were previously linked to pachynema (Luo et al., 2024). Expanded annotations and focused validation are necessary for motif-based inference to define TRN architecture during pachynema. Second, it is still unclear how enhanced chromatin accessibility, changed epigenetic alteration, XY body formation failure, and TRN disruption in Hsf5−/− pachytene spermatocytes are related. Coordinated chromatin compaction, histone modifications, LLPS, and higher-order genome organization are necessary for XY body building because they cause X and Y chromosomes to get close during meiosis (Handel, 2020; Hildebrand and Dekker, 2020). According to recent research, transcription is controlled by 3D genome-based regulatory networks that combine condensate dynamics, epigenetic states, and long-range chromatin contacts in addition to proteins binding to particular DNA sequences (Stadhouders et al., 2019; Su et al., 2020; Tian et al., 2022). A thorough mapping of the 3D genomic architecture in Hsf5−/− pachytene spermatocytes should yield important information about the complicated and sophisticated molecular mechanisms underlying the development of pachynema. Third, the molecular processes that underlie meiosis are incredibly intricate and still little understood. In order to properly illustrate the involvement of HSF5 in pachynema progression, new models will be needed for extrapolation across mammals and consideration of genetic conflicts, even if C57BL/6J mice continue to be the most practical model given current technological and experimental settings.

AVAILABLE DATA

The Genome Sequence Archive (GSA) at the National Genomics Data Center and China National Center for Bioinformation (https://ngdc.cncb.ac.cn/gsa; accession number GSA: CRA023389), Science Data Bank (https://doi.org/10.57760/sciencedb.21518), and NCBI Sequence Read Archive (SRA; https://www.ncbi.nlm.nih.gov/sra; BioProjectID PRJNA1205528). Upon reasonable request, the corresponding author will provide all additional data supporting the study's results.

ADDITIONAL INFORMATION

This article's supporting information is available online.

Rival Interests

There are no conflicting interests, according to the authors.

THE WORKS OF THE AUTHORS

C.H.L., C.X., J.F.Z., and F.S. conceived the research; C.H.L. planned, carried out, and evaluated the experiments. Bioinformatic analyses were carried out by Z.Q.Y., C.H.L., and Z.W.F.; methodology development and investigation were carried out by C.H.L., D.L.L., H.R.X., S.M.Z., X.J.Z., H.C.L., L.F.S., and Z.A.L. C.H.L. wrote the original text; Z.Q.Y., Z.W.F., and C.H.L. carried out the visualizations; all authors participated in this effort, discussed the findings, and critically reviewed and edited the manuscript. The completed manuscript was read and approved by all authors.

ACKNOWLEDGMENTS

We appreciate the insightful conversations and feedback from the Sun Laboratory members. Additionally, we acknowledge the help of Figdraw (www.figdraw.com) in the creation of Figure 6.

RESOURCES

In 2020, Abe H, Hu YC, Alavattam KG, et al. In mouse spermatogenesis, DNA damage signaling from autosomes is sequestered by the start of meiotic sex chromosome inactivation. 30(3), Current Biology, 408–420. e5.

Andreassen PR, Maezawa S, Alavattam KG, et al. 2022. The XY body and meiotic sex chromosome inactivation: a phase separation theory. 79(1): 18. Cellular and Molecular Life Sciences.

Boyle AP, Kundaje A, and Amemiya HM.

2019. Problematic genomic areas are identified by the ENCODE blacklist. 9(1): 9354 in Scientific Reports.

Blanco-Rodríguez, J. 2009. The primary spermatogenic events are shown by γH2AX. 72(11): 823–832; Microscopy Research and Technique.

Zaba LC, Giresi PG, Buenrostro JD, et al. (2013). For quick and accurate epigenomic analysis of open chromatin, DNA-binding proteins, and nucleosome location, native chromatin transposition is used. 10(12): 1213–1218 in Nature Methods.

Carrell, DT. 2008. Determining the transcriptional and translational regulatory networks involved in spermatogenesis is essential to understanding the genetics of male infertility. Journal of Andrology International, 31(5): 455–456.

Chen SF. 2023. Fastp is used for ultrafast one-pass FASTQ data preparation, quality assurance, and deduplication. e107 in iMeta, 2(2).

Goulding EH, Inselman AL, Clement TM, et al. (2015). Mice that have their spermatocytes' cyclin-dependent kinase 1 disrupted experience late meiotic arrest and sterility. Reproduction Biology, 93(6): 137.

Goldberg AL, Collins GA. 2017. The 26S proteasome's reasoning. Cell 169(5): 792-806.

Hamilton EG, Trevino AE, Corces MR, et al. 2017. An enhanced ATAC-seq procedure lowers noise and makes it possible to examine frozen tissues. 959–962 in Nature Methods, 14(10).

In 2016, Da Cruz I, Rodríguez-Casuriaga R, Santiñaque FF, et al. Transcriptome analysis of highly purified mouse spermatogenic cell populations reveals that at the pachytene stage, gene expression profiles transition from meiotic to postmeiotic activities. Genomics BMC, 17: 294.

Liang J, Dia F, Strange T, et al. 2017. Mouse spermatocytes are used to prepare meiotic chromosome spreads. Visualized Experiments Journal, (129): 55378.

Schlesinger F, Davis CA, Dobin A, et al. (2013). STAR is an ultrafast universal RNA-seq aligner. 29(1), Bioinformatics, 15–21.

Cao CC, Dong J, Wang XL, et al. 2019. In male germ cells, UHRF1 collaborates with PRMT5 and PIWI proteins and inhibits retrotransposons. 10(1): 4705 in Nature Communications.

Galán-Martínez J, Del Carmen Maza M, Berenguer I, et al. 2022. In mice, TCFL5 absence affects the transition from pachytene to diplotene during spermatogenesis. 10956 in Scientific Reports, 12(1).

Goetz P, Speed RM, Chandley AC. 1984. Meiotic prophase development in the male mouse throughout puberty: morphology and temporal sequence. Cell Science Journal, 65: 249–263.

Wang YJ, Gomes AV, Young GW, et al. 2009. The 20 S proteasome complexes in mammalian tissues exhibit contrasting proteome biology and functional variability. 302–315 in Molecular & Cellular Proteomics, 8(2).

Felipe-Medina N, Condezo YB, Gómez-H L, et al. 2019. Mouse fertility and appropriate meiotic departure depend on the spermatoproteasome's PSMA8 subunit. e1008316 in PLoS Genetics, 15(8).

Manske GL, Green CD, Ma QY, et al. 2018. an all-inclusive single-cell RNA-seq pathway for mouse spermatogenesis. 651–667 in Developmental Cell, 46(5). e10.

Wang ZQ, Guo M, Luo CH, et al. 2022. In haploid male germ cells, miRNA-dependent poly(A) length regulation uncouples transcription and translation. Dev199573, Development, 149(12).

Kyogoku H, Araki H, Hamazaki N, et al. 2021. reassembling the transcriptional network of the oocyte via transcription factors. Nature, 589 (7841), 264–269.

Lee S, Han H, Cho JW, et al. 2018. An enhanced reference library of transcriptional regulatory connections between humans and mice is called TRRUST v2. Research on Nucleic Acids, 46(D1): D380–D386.

Handel, Massachusetts. 2004. A specific meiotic chromatin domain is called the XY body.

296(1): 57–63; Experimental Cell Research.

Handel, Massachusetts. 2020. An appealing chromatin domain is the XY body. 985–987 in Biology of Reproduction, 102(5).

Hasegawa K, Maezawa S, Sin HS, et al. (2015). SCML2 controls histone H2A ubiquitination to create the male germline epigenome. 32(5): 574–588, Developmental Cell.

Heinz S, Spann N, Benner C, et al. (2010). Simple combinations of transcription factors that determine lineage prime cis-regulatory elements necessary for the identities of B cells and macrophages. 38(4), Molecular Cell, 576-589.

Dekker J, Hildebrand EM. 2020. Chromosome compartmentalization mechanisms and functions. Biochemical Sciences Trends, 45(5): 385-396.

Shen XZ, Luo CH, Hong SH, et al. 2022. Single-cell RNA sequencing is used to compare the testes of wild-type and Alkbh5-knockout mice. jkac130 in G3 Genes| Genomes| Genetics, 12(8).

Yuan J, Zhou X, Hou Y, et al. (2012). The mouse Miwi's meiosis-specific expression is controlled by USF and DNA demethylation. e1002716 in PLoS Genetics, 8(5).

Lou ZK, Ichijima M, Ichijima Y, et al. 2011. In male germ cells, MDC1 controls the chromosome-wide silence of the sex chromosomes. 959–971 in Genes & Development, 25(9).

Li H, Wysoker A, Handsaker B, et al. 2009. SAMtools and the sequence alignment/map format. 2078–2079 in Bioinformatics, 25(16).

Zheng JH, Lin ZX, Li DL, et al. 2024. Phase separation is driven in vitro by the male pachynema-specific protein MAPS, which also controls chromatin behaviors and sex body development in vivo. 113651 in Cell Reports, 43(1).

Xu HR, Yu ZQ, Luo CH, et al. 2024. Male fertility and the evolution of pachynema depend on meiotic chromatin-associated HSF5. Research on Nucleic Acids, 52(17): 10255–10275.

Zhou J, Leu NA, Luo MC, et al. (2015). During male meiosis, the polycomb protein SCML2 binds to USP7 and inhibits histone H2A ubiquitination in the XY chromatin. e1004954 in PLoS Genetics, 11(1).

El Messaoudi-Aubert S, Elderkin S, Maertens GN, et al. 2010. Polycomb control of the INK4a tumor suppressor is modulated by ubiquitin-specific proteases 7 and 11. Journal of EMBO, 29(15): 2553–2565.

Yukawa M, Alavattam KG, Maezawa S, et al. (2018). During spermatogenesis, different transcriptomes are supported by dynamic reconfiguration of open chromatin. Research on Nucleic Acids, 46(2): 593–608.

Allen GE, Nguyen KT, Miyamoto K, et al. 2018. Oocyte transcriptional reprogramming is influenced by chromatin accessibility. 304–311 in Cell Reports, 24(2).

Page J, Manterola M, De La Fuente R, et al. (2012). Which explanation—inactivation or non-reactivation—better explains why sex chromosomes remain silent during mammalian male meiosis? 307–326 in Chromosoma, 121(3).

Grüning B, Ryan DP, Ramírez F, et al. 2016. A cutting-edge web server for deep-sequencing data analysis is called deepTools2. W160–W165 in Nucleic Acids Research, 44(W1).

Bhatt SK, Qiao HY, Rao HBDP, et al. 2017. Proteases are drawn to chromosomal axes by an SUMO-ubiquitin relay in order to control meiotic recombination. 403–407 in Science, 355 (6323).

Baarends WM, Awe S, Rathke C, et al. (2014). Dynamics of chromatin during Spermiogenesis. Gene Regulatory Mechanisms, Biochimica et Biophysica Acta (BBA), 1839(3): 155–168.

Bailis JM, Roeder GS. 2000. The checkpoint for pachytene. 395–403 in Trends in Genetics, 16(9).

Teschendorff AE, Ross-Innes CS, Stark R, et al. (2012). The clinical prognosis of breast cancer is linked to differential oestrogen receptor binding. 389–393 in Nature, 481(7381).

Dormann HL, Allis CD, Shechter D, et al. 2007. Histone extraction, purification, and analysis. 1445–1457 in Nature Protocols, 2(6).

Shima JE, Mccarrey JR, Mclean DJ, et al. (2004). The transcriptome of the mouse testis: describing the expression of genes in the testis as spermatogenesis progresses. 319–330 in Biology of Reproduction, 71(1). Graf T, Filion GJ, and Stadhouders R. 2019. Cell-fate decisions are influenced by transcription factors and 3D genome conformation. 345–354 in Nature, 569(7756).

Fransz P., Tark-Dame M., and Stam M. 2019. Phase separation and loop extrusion: a function in 3D genome organization? Plant Biology Current Opinion, 48: 36–46.

Su JH, Kinrot SS, Zheng P, et al. 2020. imaging of the 3D structure and transcriptional activity of chromatin at the genome scale. 182(6), Cell, 1641–1659. e26.

Ilkhani H, Beigi Harchegani A, Tahmasbpour Marzouni E, et al. 2022. A review of epigenetic changes as a novel theory of male infertility. Fertility & Sterility International Journal, 16(1): 1–9.

Hua KJ, Tian L, Liu T, et al. 2022. The spatial arrangement of transcriptional regulatory networks in bacteria. Microorganisms, 10(12): 2366.

JMA Turner. 2015. Mammals' meiotic

silencing. Genetics Annual Review, 49: 395-412.

Erdjument-Bromage H, Wang HB, Wang LJ, et al. 2004. Polycomb silencing involves the ubiquitination of histone H2A. 873–878 in Nature, 431(7010).

Wu XL, Zhang J, Wang HQ, et al. 2024. Cell-cell communications in humans and mice mediate meiotic transcriptional reprogramming, as demonstrated by scATAC-seq and scRNA-seq. 601–616 in Zoological Research, 45(3).

Li M, Wu TZ, Wang QW, et al. 2022. using ChIPseeker to explore epigenomic datasets. e585. Current Protocols, 2(10).

Oatley MJ, Wu X, Oatley JM, et al. (2010). An essential intrinsic regulator of GDNF-induced mouse spermatogonial stem cell survival and self-renewal is the POU domain transcription factor POU3F1. 82(6): 1103–1111; Biology of Reproduction.

Luo CH, Wu XL, Hu LF, and others (2020). Analyzing azoospermic male humans for epigenomic abnormalities using transcriptome profiling, WGBS, and RNA-Seq. Journal of Genetics and Assisted Reproduction, 37(4), 789-802.

Wang WL, Tu CF, Xie CB, et al. 2022. Understanding the mechanics of meiotic recombination and its function in human reproduction, with an emphasis on non-obstructive azoospermia. Update on Human Reproduction, 28(6): 763-797.

Khan T, Zhang BB, Ma H, et al. 2020. Asthenozoospermia and flagella instability are caused by a missense variation of DNAH17. e20182365, Journal of Experimental Medicine, 217(2).

Xie W, Zheng H. 2019. the function of three-dimensional genomic structure in cell differentiation and development. 535–550 in Nature Reviews Molecular Cell Biology, 20(9).

Kleckner N, Zickler D. 2015. Meiosis involves the recombination, pairing, and synapsis of homologs. Perspectives in Biology, Cold Spring Harbor, 7(6): a016626.